ForMAX -- a beamline for multiscale and multimodal structural characterization of hierarchical materials

ForMAX - a beamline for multiscale and multimodal structural characterization of hierarchical materials

K. Nygård,[1,*] S. A. McDonald,[1] J. B. González,[1] V. Haghighat,[1] C. Appel,[1,2] E. Larsson,[1,3] R. Ghanbari,[1,4] M. Viljanen,[1] J. Silva,[1] S. Malki,[1] Y. Li,[1] V. Silva,[1] C. Weninger,[1] F. Engelmann,[1] T. Jeppsson,[1] G. Felcsuti,[1] T. Rosén,[5,6] K. Gordeyeva,[5] L. D. Söderberg,[5,6] H. Dierks,[7] Y. Zhang,[7] Z. Yao,[7] R. Yang,[7] E. M. Asimakopoulou,[7] J. K. Rogalinski,[7] J. Wallentin,[7] P. Villanueva-Perez,[7] R. Krüger,[8] T. Dreier,[8,9] M. Bech,[8] M. Liebi,[2,10,11] M. Bek,[4,12] R. Kádár,[1,4,12,13] A. E. Terry,[1] H. Tarawneh,[1] P. Ilinski,[1] J. Malmqvist,[1] and Y. Cerenius[1]

[1]*MAX IV Laboratory, Lund University, Lund, Sweden*

[2]*Paul Scherrer Institut, Villigen PSI, Switzerland*

[3]*Division of Solid Mechanics, Lund University, Lund, Sweden*

[4]*Department of Industrial and Materials Science, Chalmers University of Technology, Gothenburg, Sweden*

[5]*Department of Fibre and Polymer Technology, Royal Institute of Technology, Stockholm, Sweden*

[6]*Wallenberg Wood Science Center (WWSC), Royal Institute of Technology, Stockholm, Sweden*

[7]*Synchrotron Radiation Research, Lund University, Lund, Sweden*

[8]*Medical Radiation Physics, Lund University, Lund, Sweden*

[9]*Excillum AB, Kista, Sweden*

[10]*Institute of Materials, École Polytechnique Fédérale de Lausanne (EPFL), Lausanne, Switzerland*

[11]*Department of Physics, Chalmers University of Technology, Gothenburg, Sweden*

[12]*FibRe-Centre for Lignocellulose-based Thermoplastics, Department of Chemistry and Chemical Engineering, Chalmers University of Technology, Gothenburg, Sweden*

[13]*Wallenberg Wood Science Center (WWSC), Chalmers University of Technology, Gothenburg, Sweden*

Abstract

The ForMAX beamline at the MAX IV Laboratory provides multiscale and multimodal structural characterization of hierarchical materials in the nm to mm range by combining small- and wide-angle x-ray scattering with full-field microtomography. The modular design of the beamline is optimized for easy switching between different experimental modalities. The beamline has a special focus on the development of novel, fibrous materials from forest resources, but it is also well suited for studies within, e.g., food science and biomedical research.

*Electronic address: kim.nygard@maxiv.lu.se

I. INTRODUCTION

Many natural and synthetic materials are hierarchical, exhibiting important structure at several different length scales that govern the material's properties [1–3]. Wood is an archetypical example, with the assembly of the load-bearing cellulose at nano-, micro-, and macroscopic scales determining its mechanical properties. In order to understand the structure-function relationship in such materials, we need access to multiscale structural characterization. Moreover, we need sufficient temporal resolution to allow monitoring how the structure evolves *in situ* or *in operando* during external stimuli or processing of the material.

The ForMAX beamline of MAX IV addresses this need for structural characterization of hierarchical materials. A key feature is its modular design, that allows temporally resolved multiscale structural characterization of bulk materials owing to easy and fast switching between complementary experimental modalities: small- and wide-angle x-ray scattering (SWAXS) in the nm regime [4, 5] and full-field synchrotron x-ray microtomography (SRμCT) in the μm to mm regime [6]. Both of these techniques are applicable to a wide range of materials and suitable for temporally resolved experiments. We foresee that SWAXS will often be carried out in scanning imaging mode using a focused x-ray beam, either as SWAXS-based microscopy [7, 8], tomography [9, 10], or tensor tomography [11, 12], covering seven orders of magnitude in length scales and hence being particularly useful for structural characterization of hierarchical materials.

ForMAX is externally funded, with the objective to support research on new materials from renewable forest resources. Its construction was funded by the Knut and Alice Wallenberg foundation (kaw.wallenberg.org), while the operation costs for ten years are covered by Swedish industry via Treesearch (www.treesearch.se) - a national research platform for the development of new materials and specialty chemicals from the forest. Access for both Treesearch members and general users is granted through common calls for proposals, with half of the user beam time reserved for academic and industrial members of Treesearch. For a brief background to ForMAX, see [13].

In the following we outline the technical design of the beamline, data acquisition, and data processing, with a focus on the needs of the users. We conclude by providing a first benchmarking of the beamline and a few examples of multiscale and multimodal structural

characterization available at ForMAX.

II. TECHNICAL DESIGN

The combination of SWAXS and SRμCT provides a number of technical challenges, in particular when applied *in situ* or *in operando* to fibrous materials such as wood-based materials:

- In SRμCT one monitors the attenuated beam directly downstream of the sample (i.e., in forward scattering direction), while in SAXS one collects scattering data further downstream at small angles (typically scattering angle $2\theta < 1°$). Since the SRμCT full-field microscope blocks the view of the SAXS detector, we have devised a strategy for easy movement of the former in and out of the x-ray beam.

- WAXS from fibrous materials exhibits anisotropy, reflecting the orientation of the crystalline fibers, fibrils, or filaments. When mapping out nanoscale orientation in such materials, one needs to be able to collect WAXS data in all directions of the scattering plane [7]. In order to facilitate scanning SWAXS imaging experiments on these materials, we have therefore chosen a custom WAXS detector with a hole in the center, that passes through the SAXS signal while simultaneously catching anisotropic WAXS data.

- SWAXS is often carried out at moderate x-ray energies $E \approx 10$ keV in order to reach small scattering vector moduli q, while it is advantageous to carry out SRμCT at higher x-ray energies (≥ 20 keV) for enhanced phase contrast. As a compromise we operate ForMAX in the 8-25 keV energy range, which is particularly suitable for soft materials.

- Whereas the small divergence of the x-ray beam at the MAX IV 3 GeV storage ring [14] is beneficial for SWAXS experiments, it limits the natural beam size at the sample position in full-field imaging. As a compromise, we have placed the sample relatively far downstream of the source (42 m from source), while still allowing a reasonable sample-to-detector distance for SAXS experiments. Moreover, we will install secondary beam-expanding optics in the experimental station to facilitate full-field imaging.

- In order to obtain a clean x-ray beam for SAXS experiments, we need to reject higher harmonics of the monochromator by passing the beam via x-ray mirrors. In the full-field imaging mode, the slope errors of the mirrors cause parasitic striation of the x-ray beam. We mitigate the effect of striation by shape compensation of the mirrors.

- Due to the high photon density at fourth generation sources like the MAX IV 3 GeV storage ring [14], radiation damage in organic samples is a major issue that we need to assess and mitigate case by case. This also holds true for full-field imaging, that has traditionally been less prone to beam-induced radiation damage due to a large beam size.

- Finally, in order to accomodate various sample environments, such as a rheometer or a mechanical load device with controlled atmosphere, we need an experimental table that is spacious and has a relatively large load capacity.

In Tables I and II we summarize the main parameters of the MAX IV 3 GeV storage ring and the main components of the ForMAX beamline, respectively.

Throughout this article, we employ MAX IV's coordinate system: the lateral x axis with positive direction outbound from the ring, the vertical y axis with positive direction upwards, and the longitudinal z axis with positive direction downstream from the source. The positive direction of each rotation around the Cartesian axes (Rx, Ry, and Rz) is given by the right-hand rule.

A. Undulator and front end

ForMAX is equipped with a 3 m long room-temperature, in-vacuum undulator from Hitachi Metals. The maximum effective deflection parameter is $K = 1.89$ at the minimum magnetic gap of 4.5 mm and the measured phase error is within specification for all operational gaps. In order to cover the energy range of 8-25 keV, we make use of the fifth to thirteenth harmonics of the undulator as shown in Fig. 1. Similar to other beamlines around the MAX IV 3 GeV storage ring [15, 16], the undulator exhibits narrow harmonic peaks, $\Delta E < 100$ eV (full width at half maximum; FWHM). We summarize the main parameters of the undulator in Table III.

The front end serves as the interface between the MAX IV 3 GeV storage ring and the ForMAX beamline and was provided by Toyama. It is part of personal and machine safety systems; it ensures safe access to the optical hutch and safe equipment operation. It includes safety and photon shutters, several fixed and movable masks, various diagnostics components including beam viewers, x-ray beam position monitors, thermocouples, and vacuum gauges, as well as vacuum valves to separate different vacuum sections and to safeguard the vacuum of the storage ring in case of vacuum loss in the beamline. The fixed masks remove a vast portion of the undulator radiation power, passing through $\approx$ 130 W of radiation to the optics hutch at the projected 500 mA ring current. The movable mask, located $\approx$ 19.5 m downstream of the source, is used to define the angular acceptance of photon beam for the ForMAX beamline.

B. Primary optics

ForMAX's primary optics consist of a double crystal monochromator provided by FMB Oxford, a double multilayer monochromator by Axilon, dynamically bendable vertical and horizontal focusing mirrors in Kirkpatrick-Baez geometry by IRELEC, a photon shutter by Axilon, and four diagnostics modules by FMB Oxford that host a fixed mask limiting the beamline's acceptance angle to $\leq 24 \times 36$ μrad^2 ($x \times y$) and a high-band-pass diamond filter for heat-load management, a white-beam stop, bremsstrahlung collimators, slits, beam viewers, and beam intensity monitors. In the following we will briefly discuss the monochromators and mirrors.

1. Monochromators

Depending on the experimental needs, ForMAX can be operated using either a double crystal monochromator (DCM) or a double multilayer monochromator (MLM). In line with several other hard x-ray beamlines at MAX IV [15–17], we have chosen a horizontal deflection geometry for both monochromators to maximize their stability. In order to facilitate switching between monochromators, both employ the same fixed-exit design with 10 mm inboard offset.

The horizontally deflecting Si(111) DCM is positioned 27 m from the source. We note

that the small horizontal offset between the crystals allows for a compact and rigid design with excellent stability, as shown elsewhere [18]. In ForMAX's case, the upstream crystal is mounted directly on the Bragg goniometer (Ry) without any other motorized axes, while the downstream crystal has additional motorized adjustments for pitch Ry, roll Rz, and perpendicular motion. Moreover, the monochromator is equipped with motorized lateral x and vertical y translations. Both crystals are side cooled by clamping the crystals to liquid-nitrogen-cooled Cu blocks; the high heat load of the upstream crystal requires direct cooling of the Cu block, while indirect cooling of the Cu block by braids is sufficient to manage the lower heat load of the downstream crystal.

The horizontally deflecting MLM, in turn, is positioned 25 m from the source. While it is foreseen to be used almost exclusively for full-field imaging experiments requiring high temporal resolution, it may also find use in niche, photon-hungry scattering experiments. Both multilayer mirrors consists of flat Si(100) substrates covered with separate stripes of 200 layers of W/B_4C and 250 layers of Ru/B_4C. Each multilayer stripe has a period of ≈ 2.4 nm and ≈ 1.6 nm B_4C layer thickness, optimized for the energy range of the beamline. The bandpass of the MLM, $\Delta E/E \approx 1\%$, is larger than the width of an individual harmonic peak of the undulator. The Bragg rotation Ry of the monochromator, fine roll Rz of the upstream mirror, and fine pitch Ry of the downstream mirror are all realized by linear actuators and special flexure arrangements. Due to the large angular range of the monochromator, a longitudinal z translation of the downstream multilayer assembly is needed. Moreover, the motorized motions include the lateral x and vertical y translations of the monochromator as well as the perpendicular translation of the downstream multilayer assembly. Due to the significantly smaller Bragg angle compared to the DCM, and hence a larger x-ray beam footprint, it suffices to cool both multilayer mirrors indirectly by braids from water-cooled Galinstan baths.

2. Mirror system

The mirror system consists of vertically (VFM) and horizontally (HFM) focusing (and deflecting) mirrors in Kirkpatrick-Baez geometry, housed inside a single vacuum chamber. Each mirror works at a fixed incidence angle of 3 mrad. The mirrors serve two main purposes. First, they provide harmonic rejection. In order to cover the wide energy range of the

beamline, each mirror from Insync has three separate stripes of Si, Rh, and Pt. Second, each mirror can be independently bent to radii between ≈ 5 and 100 km, allowing us to focus at the nominal sample position or any position downstream thereof, collimate the beam, or essentially operate without focusing. In practice, the mirror bending is achieved by applying two controlled bending moments at the upstream and downstream ends of the mirror in a four-point bending configuration. Each mirror is equipped with a limited amount of stiff, motorized axes to maximize stability; lateral x and vertical y granite translation stages as well as pitch rotation (Rx for VFM, Ry for HFM) employing a high-resolution actuator and flexure parts. Moreover, the HFM is also equipped with a similar motorized roll rotation Rx by combining a high-resolution actuator and flexure parts.

Mirror slope errors cause striation of the downstream x-ray beam, that is a nuisance when operating the beamline in unfocused mode during SRμCT experiments. In order to minimize this effect, each bender is equipped with a set of five spring actuators or so-called shape compensators. The residual slope errors for the flat geometry are ≈ 0.11 and ≈ 0.13 μrad for the VFM and HFM, respectively. In the nominal elliptical shape for focusing, the mirrors show residual slope errors ≤ 0.19 μrad for each stripe.

C. Experimental station

The major components of the experimental station shown in Fig. 2 - two beam-conditioning units (BCUs), an experimental table, a detector gantry, and a flight tube - have been custom designed at MAX IV. Due to the different, and some times mutually competing, technical requirements of SWAXS and SRμCT as outlined above, we gave special attention to the integration of these components into a single instrument. Because of the modular nature of the experimental station, as described below, we have installed a dedicated PLC system to ensure its safe operation. Finally, we have dedicated space between the BCUs to assemble a setup for x-ray multi-projection imaging (XMPI) [19, 20].

1. Beam-conditioning units

The experimental station hosts two BCUs, positioned approximately 36 and 41 m downstream of the source. The upstream BCU (called BCU I) includes a fast shutter, a pneumatic

filter unit, and a set of monochromatic slits. In the near future, it will also host an x-ray prism lens that allows beam expansion in the ≈ 5 mm range for full-field tomographic imaging experiments. The downstream BCU (BCU II) includes a beam viewer, two Si diodes for x-ray beam flux monitoring, a set of monochromatic slits, and a set of compound refractive lenses optimized to provide a microfocus x-ray beam at 16.3 keV for scanning SWAXS experiments. In order to minimize the x-ray path in air for different setups, the exit vacuum window of BCU II is motorized along the beam path. Finally, all slits in the experimental station are so-called hybrid scatterless slits [21], with single crystal InP wafers mounted on tungsten carbide blades in order to suppress parasitic x-ray scattering.

2. Experimental table

The experimental table is located 42 m downstream of the source and is based on a concept developed at the ALBA synchrotron [22]. The table provides flexibility for sample environment mounting in terms of available top surface of 800×800 mm^2, load capacity of 200 kg, large lateral and vertical translation ranges of 200 mm each, and up to ≈ 520 mm space between the top surface and the x-ray beam.

The base of the experimental table is a stable and stiff granite block. For vertical y motion of the table (≈ 0.3 μm resolution [23]) we make use of two (upstream and downstream) motorized steel plates, that are driven by ball screws with linear guides and actuated by stepper motors. Flexure hinges on the steel plates allow fine tuning of the pitch Rx (20 mrad range, ≈ 0.4 μrad resolution). We have added the lateral x motion (≈ 0.3 μm resolution) on top of the assembly, again driven by a ball screw with linear guides.

3. Detector gantry

The granite detector gantry, located by the experimental table, hosts the WAXS detector and the full-field microscope for SRμCT. It has five independent motions, *viz.*,

- the longitudinal motion of the gantry along the x-ray beam path ($\approx$1500 mm range, 10 μm resolution),
- lateral ($\approx$700 mm) and vertical ($\approx$20 mm) motions of the WAXS detector (10 μm resolution each), and

- lateral (≈700 mm) and vertical (≈30 mm) motions of the full-field microscope (1 μm resolution each).

We have verified by measuring the vibrations of the microscope tip with a laser Doppler vibrometer (one minute average, integrated 4-100 Hz) that the amplitudes are < 20 nm in both lateral and vertical directions (root mean square; RMS).

The above motions permit easy and independent movement of the WAXS detector and the full-field microscope in and out of the x-ray beam, thus providing a number of different experimental modes:

- In the SWAXS setup (see Fig. 2), we center the x-ray beam on the WAXS detector, while the SAXS signal (and unscattered beam) passes through the central hole of the WAXS detector and impinges on the SAXS detector (and the central beam stop). In this setup, we translate the full-field microscope out of the x-ray beam path. In the SAXS setup, in turn, we also translate the WAXS detector out of the x-ray beam path and mount an evacuated nose cone onto the flight tube to minimize the air path downstream of the sample.

- In the SRμCT setup, we translate the WAXS detector out of the path of the x-ray beam. As a safety measure we close a gate valve at the entrance of the flight tube, to avoid x-ray exposure of the SAXS detector.

- In the combined SAXS and SRμCT setup, we align the SAXS detector with the x-ray beam, and translate the full-field microscope vertically in and out of the x-ray beam path for full-field imaging and scattering modes, respectively. The vertical translation of the microscope out of the x-ray beam path takes ≈ 15 seconds. A combined SWAXS and SRμCT setup is also possible, but the accessible SAXS and WAXS angular ranges are limited by space restrictions.

4. Flight tube

In order to minimize (i) absorption of the scattered x-ray beam and (ii) parasitic x-ray scattering from air, we have placed the SAXS detector on a motorized detector trolley inside a 9 m long and 1 m diameter evacuated vacuum vessel operating at $\approx 10^{-3}$ mbar. We have

also mounted a motorized central beam stop, made from tungsten and equipped with a GaAs diode for monitoring the flux of the transmitted x-ray beam, on the detector trolley. The motorized longitudinal motion of the detector trolley permits easy switching of the nominal sample-to-detector distance in the range of $\approx 800 - 7600$ mm [24], while the independent motorized lateral and vertical motions allow users to freely position the SAXS detector with respect to the direct x-ray beam. We have mechanically decoupled the rail system of the detector trolley from the vacuum vessel, thereby isolating the trolley motion from vibrations and vacuum-induced deformations of the vessel.

D. Sample manipulation

ForMAX offers a number of experimental techniques, each with specific requirements with respect to sample manipulation. In order to meet different user needs, ForMAX is equipped with three separate stacks of stages for sample manipulation:

- For SWAXS experiments, we provide a high-load (≤ 1500 N) five-axis assembly from Huber as shown in Fig. 3A. It consists, from bottom to top, of motorized pitch Rx ($\pm 13°$), roll Rz ($\pm 12°$), lateral x (± 25 mm), longitudinal z (± 25 mm), and vertical y (± 20 mm) axes. In order to simplify mounting of sample holders or environments, we have added an optical breadboard with a 25×25 mm^2 grid of centered ISO metric M6 threaded holes on top of the stages. The nominal distance between the top surface and the center of rotation is 49 ± 20 mm, but this can be increased owing to the modular nature of the assembly of stages.

- For scanning SWAXS experiments, we provide another assembly with five degrees of freedom by Huber, see Fig. 3B. The base consists of motorized lateral x (± 25 mm), vertical y (± 10 or ± 45 mm, depending on resolution and speed requirements), and longitudinal z (± 25 mm) axes for 2D scanning and adjustment of the sample along the x-ray beam path. On top of these we have mounted a yaw Ry axis that, combined with the translation stages below, allows SWAXS tomographic imaging. Finally, we have added a large-range, custom pitch axis Rx ($\pm 45°$) for SWAXS tensor tomography experiments. A manual five-axis goniometer head on top of the assembly enable fine alignment of the sample.

- In SRμCT experiments we employ a five-axis assembly from Lab Motion as shown in Fig. 3C. It consists, from bottom to top, of a motorized longitudinal z axis ($\approx$ 380 mm range) for propagation-based phase-contrast imaging, a vertical y axis ($\pm$20 mm) for helical imaging, an air-bearing tomographic yaw axis Ry, coupled with a rotary union accomodating a fluid slip ring, and horizontal xz axes ($\pm$5 mm each) for sample alignment. The electrical slip ring is equipped with 15 spare wires for integration of sample environments. The maximum rotation speed of the yaw stage is 720 revolutions per minute, allowing SRμCT experiments with temporal resolution up to $\approx$ 20 Hz. The assembly is modular and is typically operated without the vertical axis and the rotary union. In order to facilitate mounting of sample holders or environments, we have installed an optical breadboard with a 12.5 $\times$ 12.5 mm^2 grid of centered ISO metric M6 threaded holes on top of the stages.

We further note that we can combine the air-bearing tomographic rotation stage with linear scanning SWAXS stages in a modular setup, allowing combined high-resolution SRμCT and 2D/3D scanning SWAXS experiments without the need to re-mount the sample upon changing experimental modality.

III. DATA ACQUISITION AND PROCESSING

Data acquisition and processing greatly affects the user experience. In the following, we briefly review how these are managed at the ForMAX beamline.

A. X-ray detection systems

For SWAXS experiments, ForMAX is equipped with two megapixel, hybrid photon-counting detectors that provide high resolution, high dynamic range, and low noise. The SAXS detector is a vacuum-compatible Dectris EIGER2 X 4M [25]. The WAXS detector, in turn, is a custom X-Spectrum Lambda 3M [26]. In Table IV we provide technical details about both detectors.

The range of scattering vector modulus q covered by the SAXS detector depends on the x-ray energy, sample-to-detector distance (SDD), positioning of the SAXS detector in the scattering plane, and the size of the central beam stop (at the moment 4-5 mm diameter);

assuming that the SAXS detector is centered on the direct x-ray beam, the accessible SAXS q range varies from $q \approx 0.01 \ldots 0.5$ nm^{-1} at minimum x-ray energy and maximum SDD to $q \approx 0.25 \ldots 10$ nm^{-1} at maximum energy and minimum SDD.

The custom WAXS detector warrants a more detailed discussion. In order to facilitate scanning SWAXS experiments from fibrous materials, it has a hole in the center to pass through the SAXS signal (and the direct x-ray beam), while simultaneously allowing us to collect WAXS data in all directions of the scattering plane as exemplified in Fig. 4A. Moreover, it is mounted onto an evacuated nose cone and connected to the flight tube via a bellow, thereby minimizing parasitic air scattering in the SAXS regime. At the nominal SDD of 135 mm, we can collect WAXS data at scattering angles $2\theta = 7 \ldots 20^\circ$ in all directions of the scattering plane, yielding the energy-dependent range of accessible scattering vector moduli $q = (4\pi/\lambda)\sin(\theta)$ shown in Fig. 4B. We note that there is $\approx$ 100 mm path of air between the sample and the entrance window of the flight tube when using the WAXS detector, adding to the parasitic background scattering in the SAXS regime. Finally, due to the thickness of the full-field microscope, SDD$\geq$ 235 mm in the combined SWAXS and SRμCT experiments, essentially halving (i) the energy-dependent minimum and maximum q of Fig. 4B and (ii) the accessible scattering angles 2θ in the SAXS regime due to shadowing of the flight tube entrance window, hence in practice limiting these experiments to x-ray energies $\geq$ 20 keV.

For SRμCT experiments, ForMAX is equipped with a high-resolution full-field microtomography detection system encompassing two main components − an optical microscope and a sCMOS camera. The transmitted x-ray beam is converted by a scintillator into visible light, that in turn is magnified by the optical microscope and recorded by the sCMOS camera. The white-beam optical microscope from Optique Peter has motorized triple objective lens and dual camera port configurations for simple switching of magnification and sCMOS camera, respectively. We can operate the microscope with 2×, 5×, 7.5×, 10×, and 20× objectives, depending on the required effective pixel size and field of view.

Currently we employ two sCMOS cameras for high-resolution imaging at limited speed, the Hamamatsu ORCA Lightning and the Andor Zyla. We are also in the process of acquiring a high-speed Photron FASTCAM Nova sCMOS camera to allow $\approx$ 20 Hz SRμCT, i.e., the maximum temporal resolution allowed for by the tomographic rotation stage. We summarize the technical details of the sCMOS cameras in Table V.

We have evaluated the performance and resolution of the presented SRμCT system. For this evaluation, we used the full-field microscope with 5×, 10×, and 20× magnification coupled to the Andor Zyla camera (physical pixel size 6.5 μm), resulting in 1.3, 0.65, and 0.325 μm effective pixel size, respectively. The reconstructed slices for the different magnifications of a wood sample are presented in the right column of Fig. 5. We also evaluated the resolution over the 3D reconstructed volume using the Fourier Shell Correlation (FSC) together with the half-bit threshold criterion [27, 28] as depicted in the right column of Fig. 5. We observe that the ForMAX instrument retrieves Nyquist-limited resolution for the 5× and 10× magnifications, i.e., 2.6 and 1.3 μm resolution. For the 20× magnification, the retrieved resolution was around 3 pixels, which corresponds to 0.975 μm. Thus, the ForMAX instrument is ideal to characterize objects in 3D with micrometer and submicrometer resolution.

B. Control system

ForMAX's control system is based on Tango [29], an open-source control system that is in use at several European synchrotron facilities. On top of Tango we employ Sardana [30], a software environment for, e.g., controlling motors, acquiring signals, and running macros. We have optimized the scan routines for the specific needs of ForMAX, such as reducing the overhead per line in continuous xy mesh scans to < 1 second for scanning SWAXS applications. From a hardware point of view, the majority of our motorized axes are based on stepper motors controlled by IcePAP [31] and we make use of PandABoxes for synchronization of the experiments [32].

C. Data pipelines

All detectors are integrated into the beamline control system via dedicated detector servers, utilizing detector-specific software development kits (SDKs) running on detector control units (DCUs) for detector control and data readout. Low-level image processing such as flat-field correction is either applied by default (for hybrid pixel detectors; SWAXS) or in the image reconstruction (for sCMOS cameras; SRμCT), while low level acquisition parameters such as acquisition time, number of frames, and photon-counting threshold en-

ergy are accessible to the user. Finally, the data are streamed via high-speed Ethernet connections to MAX IV's central data storage [33] and saved together with metadata in the hierarchical data format 5 (HDF5).

In parallel with data streaming and storage of the as measured scattering data, our SWAXS data pipeline reduces the data to a more user-friendly format. The data reduction is carried out using the python implementation of *MatFRAIA* [34], based on a matrix-multiplication algorithm for radial and azimuthal integration, and is faster than the maximum frame rate of the EIGER detector. We reduce the SWAXS data into both 1D $I(q)$ and 2D $I(q, \varphi)$ formats, where I denotes the scattering intensity and φ the azimuthal angle. We emphasize that the fast data reduction into so-called 'cake plots', $I(q, \varphi)$, is particularly convenient for monitoring anisotropic scattering from fibrous materials in (scanning) SWAXS experiments. For calibration and masking of the detectors we utilize *PyFAI* [35], which is well known in the user community. Finally, in order to facilitate monitoring of the experiment, we plot either the radial integral $I(q)$ or the 'cake plot' $I(q, \varphi)$ in both SAXS and WAXS regimes in live mode. In Fig. 6 we present a snapshot from the beamline control computer, exemplifying the live plotting of reduced SWAXS data.

In SRμCT experiments, we take a different approach for the data pipeline. In line with community convention, we collect projections as well as flat- and dark-field images using dedicated scan routines and save all data in common HDF5 files. In order to further improve user friendliness, we are currently in the process of implementing live tomographic reconstructions for SRμCT experiments.

D. Data analysis and image reconstructions

ForMAX allows a wide range of SWAXS, scanning SWAXS, and SRμCT experiments, each with their unique requirements with respect to on-line data analysis. In order to support all these different experiments, we provide up-to-date *Jupyter notebook* templates for our users. For SRμCT experiments, the script for tomographic reconstruction includes the option to perform phase retrieval for single-distance propagation-based phase contrast tomography, in addition to standard absorption contrast tomography reconstruction. We plan to continuously implement further developments, including the aforementioned live tomographic reconstructions for SRμCT experiments.

SAXS tensor tomography (SASTT), that combines concepts of scanning SAXS with SRμCT to retrieve not solely scattering intensity measures but the full 3D reciprocal space map within each voxel of the tomogram, is a special case due to the high demands on image reconstruction. Data acquisition must be matched with sufficient computational resources to allow reconstructions of the 3D reciprocal space map, ideally already during the experiment, to evaluate the quality of the measurements. At ForMAX, we have implemented *Jupyter notebook* templates for projection alignment and apply the software package *Mumott* (mumott.org) to perform SASTT reconstructions. In the future, we plan to continuously update these notebooks to remain up to date and match further developments and improvements of the reconstruction algorithm. Details about *Mumott* can be found in a recent publication [36].

IV. BENCHMARKING

In this section we report on initial benchmarking of the main x-ray beam properties at ForMAX.

A. Beam size

The dynamically bendable mirrors provide means to vary the lateral and vertical beam size at the sample position in a large range. In the unfocused mode, we obtain an FWHM beam size of $\approx 0.8 \times 1.3$ mm^2 ($x \times y$) using the DCM, while the larger bandpass of the MLM yields a beam size of $\approx 1.3 \times 1.5$ mm^2. In the other extreme, we can focus the beam down to $\approx 55 \ldots 60 \times 10 \ldots 15$ μm^2 at the sample position using either monochromator. In this case, the lateral beam size is limited by source size and imaging geometry, while the vertical beam size is limited by slope errors of the mirrors.

In order to further decrease the beam size at the sample position, we have installed compound refractive lenses (CRLs) $\approx$ 1.5 m upstream of the nominal sample position. At the moment we employ a stack of 16 radiation-resistant SU-8 polymeric lenses from Microworks, optimized for 16.3 keV x-rays and yielding a FWHM beam size of $\approx 10 \times 2$ μm^2 at the sample position. This is similar to the beam size typically available at third-generation SWAXS beamlines with microfocus capability [37, 38].

The natural beam size at ForMAX limits SRμCT experiments on large samples. This limitation can be partly overcome by stitching images, but at the expense of temporal resolution. We will soon also install an optional, overfocusing SU-8 x-ray prism lens from Microworks ≈ 5.4 m upstream of the nominal sample position, yielding an energy-dependent x-ray beam size of $\approx 5 \times 5$ mm^2 or larger at the sample position in combination with the DCM.

B. Flux

The imaging techniques available at ForMAX rely on a large incident photon flux. In Fig. 7 we present the x-ray photon flux at the sample position, as measured using both monochromators. We collected the data at ≈ 9 and 20 keV, corresponding to the energy of the fifth and eleventh undulator harmonics at minimum gap. These energies were selected to ensure sufficient harmonic rejection with the Si and Rh stripes of the mirrors, respectively, while attenuating the x-ray beam and measuring the x-ray flux using the EIGER detector. The measured fluxes agree within a factor of three with results based on ray-tracing simulations with *XRT* [39], assuming ideal undulator and optics. For comparison we also present the flux of two competitive beamlines at third generation synchrotron sources of comparable size to MAX IV: the I22 SWAXS beamline at Diamond Light Source [38] and the TOMCAT SRμCT beamline at the Swiss Light Source [40] (see also www.psi.ch/en/sls/tomcat).

In terms of SWAXS, the photon flux at ForMAX using the DCM is comparable to the one at beamline ID02 of the European Sychrotron Radiation Facility after their accelerator upgrade [41], about an order of magnitude larger than the flux at I22. Moreover, the MLM is available for niche experiments requiring an even higher flux. In terms of SRμCT, in turn, the flux using the MLM is comparable to the one available at TOMCAT, albeit in a two orders of magnitude smaller beam cross section. We note that while the small beam size at ForMAX limits the capability of full-field imaging of large samples, as alluded to above, the very high photon density instead carries the potential for ultrafast imaging.

C. Coherence estimation

In this section, we estimated the coherent effects present in in-line holography at the ForMAX beamline. Specifically, we evaluated the effects of the coherence in the formation of holographic fringes. We envision performing an exhaustive estimation of the coherence of ForMAX [42, 43] for different energies and imaging configurations, but this is out of the scope of the present paper.

We performed in-line holography at 9.1 keV, imaging a broken Si_3N_4 membrane that exhibited several sharp edges with random orientations [44]. Fig. 8A depicts the hologram (I) recorded 19 cm downstream of the sample, using the SRμCT detection system with an effective pixel size of 0.325 μm and a response function (also known as the Point Spread Function; PSF) with a FWHM corresponding to 3 pixels (σ_{PSF}=0.41 μm), as estimated in section III A for the 20x magnification objective. The Fourier transform of the recorded hologram ($\hat{I}$) can be written as [45]

$$\hat{I} = \left[\delta(f) + 2\hat{\phi}\sin(\pi\lambda z f^2)\right]\hat{R}(f)\gamma_C(f), \tag{1}$$

where f is the frequency, ϕ the wave's phase after the object, λ the wavelength, z the propagation distance between the sample and the detector, R the detector's point-spread function, and γ_C the degree of coherence. The sinusoidal term in Eq. (1) is also known as the contrast-transfer function [46] and the visibility of its oscillations as a function of the frequency is limited by the coherence and the PSF. The power spectrum ($|\hat{I}|^2$) of the recorded hologram in logarithmic scale is depicted in Fig. 8B. We clearly observe an asymmetry between the visibility of the CTF oscillations in the vertical and lateral directions due to coherent effects.

To study the coherence effects in a more quantitative manner, we performed a fit of Eq. (1) to the power spectrum, describing the PSF and the degree of coherence by a Gaussian function with the standard deviation

$$\sigma_{\mathrm{TOT}=\sqrt{\sigma_{\mathrm{PSF}}^2+\sigma_C^2}}, \tag{2}$$

where σ_C is due to the degree of coherence. Because of the difference in phase space of the source in the principal directions, we fitted the data independently in vertical and lateral directions. On the one hand, the vertical $\sigma_{\mathrm{TOT}} \approx 0.40$ μm is compatible with the blurring

due to the PSF. Thus, the visibility of the fringes in the vertical direction is limited by the PSF. On the other hand, the lateral $\sigma_{\mathrm{TOT}} \approx 0.71$ μm corresponds to $\sigma_C \approx 0.58$ μm. Therefore, the lateral visibility is mainly limited by the degree of coherence, as expected by the ForMAX source parameters of Table I. Fig. 8C depicts the angular average of the power spectrum and the best-fit result to estimate the degree of coherence for the vertical and horizontal components.

D. SAXS contrast

Parasitic scattering in the small-angle regime hampers SAXS studies of weakly scattering, biobased materials, such as low-concentration suspensions of cellulose nanoparticles. In order to mitigate this effect, all windows in the x-ray beam path of the ForMAX beamline are single crystalline.

In Fig. 9 we show SAXS data $I(q)$ collected using 12.7 keV x-rays and an SDD of $\approx$ 2 m from highly charged, TEMPO-oxidized cellulose nanofibrils dispersed in water at a low concentration of 0.3 weight-%. In order to highlight the effect of parasitic scattering, we present the data as the scattering contrast $[I(q) - I_{bg}(q)]/I_{bg}(q)$, where $I_{bg}(q)$ denotes scattering from the water-filled sample cell. For comparison, we also show corresponding data collected at the LiX beamline of NSLS-II [47]. Although these data have been collected from different samples and using different window materials of the sample cell (cyclic olefin copolymer at ForMAX versus mica at LiX), they demonstrate that the SAXS contrast at ForMAX is at a comparable high level to that of a modern SAXS beamline optimized for solution scattering.

V. PROBING HIERARCHICAL MATERIALS

The objective of the ForMAX beamline is to provide multiscale and multimodal structural characterization of materials from nm to mm length scales. In the following, we demonstrate this capability with a few examples.

A. Combined scanning SWAXS and SRμCT

A key feature of ForMAX is the possibility of zooming into hierarchical materials, as illustrated in Fig. 10. In a first instance, we acquire a high-resolution 3D image by SRμCT, yielding microscopic structural characterization of the sample. This is exemplified in Fig. 10A for a sample of aspen sapling mounted in tangential geometry. Moreover, the tomogram allows us to identify regions of interest (RoI) for scanning SWAXS mapping of nanoscale structures. In the second instance, we focus the x-ray beam onto the sample position and collect spatially resolved SWAXS data on either the RoIs or the full sample, as illustrated in Figs. 10B and C-D for SAXS and WAXS, respectively. We note that whereas the SAXS and WAXS data of Figs. 10 provide access to structural properties such as microfibril size and orientation, the WAXS data of Figs. 10C and D also allow the mapping of other crystalline compounds within the sample, in this case calcium oxalate crystals. For bio-based materials, different crystalline agents are often present in the samples, and with the combination of spatial SRμCT and SWAXS data, the regions of interest within the sample can be reconstructed using various scattering contrasts.

The feature of zooming into hierarchical materials is still under development. Potential means for improving user friendliness include, e.g., a graphical user interface for selecting RoIs from the 3D SRμCT data. Nevertheless, ForMAX provides already in its present state unique means for multiscale and multimodal structural characterization of soft and/or bio-based materials in the nm to mm range.

B. SAXS tensor tomography

As noted in the introduction, scanning SWAXS imaging provides structural characterization across seven orders of magnitude in length scales in a single experiment. SAXS tensor tomography (SASTT) is particularly useful for hierarchical materials, since the statistically averaged local orientation of fibrils, fibers, or filaments accessible in these experiments is directly linked to the mechanical properties of the sample. In the scope of commissioning the beamline, we acquired a SASTT dataset from carbon fiber bundles that were carefully arranged in the shape of a small knot. A similar test sample has already been used in the initial SASTT commissioning experiments at the cSAXS beamline, Swiss Light Source

[11]. The purpose of such a measurement is to ensure the proper mapping of 3D reciprocal space (scattering directions) and real space directions, xy scanning at different rotation and tilt orientations, into the reconstruction algorithm. We successfully reconstructed the first dataset already during the beamtime, due to the readily available computing resources at the MAX IV high performance cluster (HPC).

The input for the reconstruction consists of a dataset with 276 two-dimensional projections with 55×76 pixels ($x \times y$) at a pixel size of 25 μm, computed from a total of 1.15M detector frames. Each pixel of every projection consists of detector data which was reintegrated into 32 azimuthal bins in the range of $q = 0.3 \ldots 0.5$ nm^{-1} and further symmetrically averaged to remove detector gaps. The remaining 16 azimuthal bins are used as input for the SASTT reconstruction with *Mumott* version 1.2 (https://zenodo.org/records/8404162). Another important step in the workflow is projection alignment. We used a computational procedure to align all projections for different orientations of the sample ($Rx = 0 \ldots 180°$ for $Ry = 0°$, $Rx = 0 \ldots 360°$ for $Ry > 0°$), that first generates a tomogram for $Ry = 0°$ and next back projects the projections of all other tilts and uses *phase_cross_correlation* from the *skimage.registration* python package for image registration and computation of the required shifts. We used the integrated dark field signal as input for the alignment procedure, due to the weak absorption signal from the carbon fibers. The same procedure was further used to mask out the sample holder and frame from some of the projections. The computed vertical and horizontal shifts are in total ≤ 200 μm (see Fig. 11), showing that the experimental setup is very stable.

We reconstruct the 3D reciprocal space in each voxel using band-limited Friedel symmetric spherical functions expressed in spherical harmonics up to a maximum order of 6, which results in 28 coefficients for each voxel that are used to reconstruct the 3D reciprocal space. The orientation of the main structure is determined from the eigenvector associated with the smallest eigenvalue of the rank-2 tensor. We have checked the robustness of the reconstruction by visual comparison of 2D orientation, anisotropy, and degree of orientation between the measurements and simulated projections of the reconstructed data. Finally, we calculate the degree of orientation as the ratio between the mean (isotropic component) and standard deviation (RMS of anisotropic component).

We display the results of the reconstruction in Fig. 12. In Fig. 12A, we directly compare the input data of the mean intensity with a synthetic projection computed from results of

the reconstruction. Since there is essentially no difference between measured and synthetic projections, which is the goal of the reconstruction, we move on to inspect the tomogram in more detail. Fig. 12B displays two central cuts, a *zx* and a *zy* slice through the tomographic reconstructed mean intensity, which gives direct insights into the arrangement of the fibers within the knot. The top left of the image exhibits a region of higher intensity where the fiber bundles from top/bottom overlap, while the opposing side of the image shows two open loops of less densely packed material. Besides the mean intensity, SASTT reconstructions also offer the unique possibility to assess the 3D reciprocal space map within each voxel, as shown in Fig. 12C for selected voxels of the tomogram (scaled with the same colormap for better comparison). The high intensity region clearly shows a ring-like reciprocal space map, which is expected for fiber-like structures. Finally, in Fig. 12D we visualize the combined information of the carbon fiber knot using the visualization software *ParaView* (www.paraview.org). Cylinder glyphs with fixed aspect ratio point in the direction of the carbon fibers. We use the mean intensity, a measure of the material's density, to scale as well as color-code the glyphs. Note that we have masked the output with a 3D array taken from the mean intensity to exclude low scattering regions and mask out data from air/background voxels.

C. Advanced rheological and mechanical testing

In situ rheological or mechanical testing is a common approach to address, for example, flow-induced assembly of nanoparticles into advanced materials or the relationship between structural and mechanical properties in fibrous materials. We foresee that such studies will be popular among our user community. However, while combined rheological and small-angle scattering experiments are rather mature [48], a deep understanding of flow-induced assembly of nanoparticle suspensions into novel hierarchical materials requires simultaneous rheological and multiscale structural characterization [49, 50]. This is particularly important for the assembly and development of new materials from biomass, for which the importance of flow cannot be overstated. Likewise, while *in situ* uniaxial tensile or compressional load is commonly excerted during SWAXS or SRμCT experiments, materials engineering applications may require more complex load geometries and loading profiles or extensive load cycling in well controlled temperature and relative humidity. Again, this is of great importance for

biobased materials, that are viscoelastic even in their solid state.

In parallel with the construction and commissioning of ForMAX, we have therefore also developed x-ray methodology to further expand the possibilities for multiscale and multimodal structural characterization during rheological and mechanical testing. Based on this development work we can, together with our sister beamline CoSAXS [17], provide users with the following capability:

- Simultaneous rheological and SWAXS experiments, as exemplified in Figs. 13A and 13C for a cellulose nanocrystal suspension subjected to laminar Couette flow in a concentric polycarbonate cup-bob geometry. Other geometries, including plate-plate geometry that allows simultaneous mesoscale structural characterization by polarized light imaging (see Fig. 13D), and environmental control are also available. Finally, we note that the MLM provides the prospect of supreme temporal resolution in such studies.

- We're addressing the need for more complex *in situ* load experiments by developing combined dynamical mechanical analysis (DMA) and SWAXS in an atmosphere of controlled temperature and humidity, see Fig. 13B. Inspired by recent development of combined rheological and SRμCT experiments [51], we're currently expanding the DMA-SWAXS experiments towards multiscale structural characterization by introducing simultaneous SRμCT capability, using the rheometer in co-rotation mode as the tomographic rotation stage.

VI. CONCLUSIONS AND OUTLOOK

We have recently brought into operation ForMAX, that allows unique multiscale and multimodal structural characterization of hierarchical materials in the nm to mm range by combining SWAXS, scanning SWAXS imaging, and SRμCT (or any combination of these techniques) in a single experiment. Although we are still optimizing the beamline's performance, the initial benchmarking of the x-ray beam properties reported here demonstrates ForMAX's potential.

A major aspect of ForMAX is the possibility to monitor multiscale structural evolution during material processing. Currently we are developing this possibility along two different

paths. First, the very high photon density at ForMAX provides unprecedented possibilities for ultrafast full-field imaging. Second, we are working on dedicated sample environments that allow multiscale structural characterization during complex rheological or mechanical testing under controlled temperature and humidity, as exemplified above. We hope to make these developments available for general users in the near future.

We thank the staff at the MAX IV Laboratory for all their support during the beamline project. The construction of ForMAX has been funded by the Knut and Alice Wallenberg Foundation, while a large fraction of the operation costs are covered by Swedish industry via the Treesearch platform. Research conducted at MAX IV, a Swedish national user facility, is supported by the Swedish Research Council under contract 2018-07152, the Swedish Governmental Agency for Innovation Systems under contract 2018-04969, and Formas under contract 2019-02496. We have received additional funding from the European Union's Horizon 2020 Framework Programme via the European Research Council (WIREDIRECT, grant agreement 801847; 3DX-FLASH, 948426; MUMOTT, 949301) and the Marie Sklodowska-Curie Actions (PSI-FELLOW-III-3i, grant agreement 884104), the Swedish Research Council (project grant number 2022-04192), the Swedish Foundation for Strategic Research (SSF grant ID17-0097), the Crafoord foundation, NanoLund, the 'FibRe - Competence Centre for Design for Circularity: Lignocellulose- based Thermoplastics' partly funded by the Swedish Innovation Agency VINNOVA (Grant Number 2019-00047), Chalmers Center for Advanced Neutron and X-ray scattering techniques, and Chalmers Area of Advance Materials Science.

---

[1] R. Lakes, Nature **361**, 511 (1993).

[2] P. Fratzl and R. Weinkamer, Prog. Mat. Sci. **52**, 1263 (2007).

[3] L. J. Gibson, J. R. Soc. Interface **9**, 2749 (2012).

[4] O. Glatter and O. Kratky, eds., *Small-Angle X-ray Scattering* (Academic Press, 1982).

[5] B. R. Pauw, J. Phys.: Condens. Matter **25**, 383201 (2013).

[6] E. Maire and P. J. Withers, Int. Mater. Rev. **59**, 1 (2014).

[7] H. Lichtenegger, M. Müller, O. Paris, C. Riekel, and P. Fratzl, J. Appl. Cryst. **32**, 1127 (1999).

[8] O. Bunk, M. Bech, T. H. Jensen, R. Feidenhans'l, T. Binderup, A. Menzel, and F. Pfeiffer, New J. Phys. **19**, 123016 (2009).

[9] J. M. Feldkamp, M. Kuhlmann, S. V. Roth, A. Timmann, R. Gehrke, I. Shakhverdova, P. Paufler, S. K. Filatov, R. S. Bubnova, and C. G. Schroer, Phys. Status Solidi A **206**, 1723 (2009).

[10] T. H. Jensen, M. Bech, O. Bunk, M. Thomsen, A. Menzel, A. Bouchet, B. Le-Duc, and F. Pfeiffer, Phys. Med. Biol. **56**, 1717 (2011).

[11] M. Liebi, M. Georgiadis, A. Menzel, P. Schneider, J. Kohlbrecher, O. Bunk, and M. Guizar-Sicairos, Nature **527**, 349 (2015).

[12] F. Schaff, M. Bech, P. Zaslansky, C. Jud, M. Liebi, M. Guizar-Sicairos, and F. Pfeiffer, Nature **527**, 353 (2015).

[13] J. McEntee, Physics World Instrum. Vac. Briefing pp. 5–8 (2023).

[14] P. F. Tavares, E. Al-Dmour, Å. Andersson, F. Cullinan, B. N. Jensen, D. Olsson, D. K. Olsson, M. Sjöström, H. Tarawhen, S. Thorin, et al., J. Synchrotron Rad. **25**, 1291 (2018).

[15] T. Ursby, K. Åhnberg, R. Appio, O. Aurelius, A. Barczyk, M. Bjelčić, F. Blomsten, Y. Cerenius, R. B. Doak, M. Eguiraun, et al., J. Synchrotron Rad. **27**, 1415–1429 (2020).

[16] U. Johansson, D. Carbone, S. Kalbfleisch, A. Björling, M. Kahnt, S. Sala, T. Stankevic, M. Liebi, A. R. Fernandez, B. Bring, et al., J. Synchrotron Rad. **28**, 1935 (2021).

[17] M. Kahnt, K. Klementiev, V. Haghighat, C. Weninger, T. S. Plivelic, A. E. Terry, and A. Björling, J. Synchrotron Rad. **28**, 1948 (2021).

[18] P. Kristiansen, U. Johansson, T. Ursby, and B. N. Jensen, J. Synchrotron Rad. **23**, 1076 (2016).

[19] P. Villanueva-Perez, B. Pedrini, R. Mokso, P. Vagovic, V. A. Guzenko, S. J. Leake, P. R. Willmott, P. Oberta, C. David, H. N. Chapman, et al., Optica **5**, 1521 (2018).

[20] P. Villanueva-Perez, V. Bellucci, Y. Zhang, S. Birnsteinova, R. Graceffa, L. Adriano, E. M. Asimakopoulou, I. Petrov, Z. Yao, M. Romagnoni, et al., arXiv p. 2305.11920 (2023).

[21] Y. Li, R. Beck, T. Huang, M. C. Choi, and M. Divinagracia, J. Appl. Cryst. **41**, 1134 (2008).

[22] C. Colldelram, C. Ruget, and L. Nikitina, Proc. MEDSI'10 **1**, e44 (2010).

[23] Throughout this paper, we define the resolution of mechanical components as the minimum incremental motion per full step.

[24] Depending on the setup, the SAXS detector may be partially shadowed at short sample-to-detector distances.

[25] T. Donath, D. Š. Jung, M. Burian, V. Radicci, P. Zambon, A. N. Fitch, C. Dejoie, B. Zhang, M. Ruat, M. Hanfland, et al., J. Synchrotron Rad. **30**, 723 (2023).

[26] D. Pennicard, S. Lange, S. Smoljanin, H. Hirsemann, H. Graafsma, M. Epple, M. Zuvic, M. O. Lampert, T. Fritzsch, and M. Rothermund, J. Phys.: Conf. Series **425**, 062010 (2013).

[27] M. van Heel, Ultramicroscopy **21**, 95 (1987).

[28] M. van Heel and M. Schatz, Journal of structural biology **151**, 250 (2005).

[29] J.-M. Chaize, A. Götz, W.-D. Klotz, J. Meyer, M. Perez, and E. Taurel, in *Proceedings of the 7th International Conference on Accelerator and Large Experimental Physics Control Systems (ICALEPCS'99)* (1999), pp. 475–479.

[30] T. Coutinho, G. Cuní, D. Fernández-Carreiras, J. Klora, C. Pascual-Izarra, Z. Reszela, R. Suñé, A. Homs, E. Taurel, and V. Rey, in *Proceedings of the 13th International Conference on Accelerator and Large Experimental Physics Control Systems (ICALEPCS 2011)* (2011), pp. 607–609.

[31] N. Janvier, J. M. Clement, P. Fajardo, and G. Cuní, in *Proceedings of the 14th International Conference on Accelerator and Large Experimental Physics Control Systems (ICALEPCS 2013)* (2013), pp. 766–769.

[32] S. Zhang, Y. M. Abiven, J. Bisou, G. Renaud, G. Thibaux, F. Ta, S. Minolli, and F. Langlois, in *Proceedings of the 16th International Conference on Accelerator and Large Experimental Physics Control Systems (ICALEPCS 2017)* (2017), pp. 143–150.

[33] In the case of the high-speed Photron sCMOS camera, the data will temporarily be saved on the local data storage of the camera, before transfer to the central data storage.

[34] A. B. Jensen, T. E. K. Christensen, C. Weninger, and H. Birkedal, J. Synchrotron Rad. **29**, 1420 (2022).

[35] J. Kieffer, S. Petitdemange, and T. Vincent, J. Synchrotron Rad. **25**, 612 (2018).

[36] L. M. Nielsen, P. Erhart, M. Guizar-Sicairos, and M. Liebi, Acta Cryst. **A79**, 515 (2023).

[37] A. Buffet, A. Rothkirch, R. Döhrmann, V. Körstgens, M. M. A. Kashem, J. Perlich, G. Herzhog, M. Schwartzkopf, R. Gehrke, P. Müller-Buschbaum, et al., J. Synchrotron Rad. **11**, 647 (2012).

[38] M. J. Smith, S. G. Alcock, L. S. Davidson, J. H. Emmins, J. C. H. Bardsley, P. Holloway, M. Malfois, A. R. Marshall, C. L. Pizzey, S. E. Rogers, et al., J. Synchrotron Rad. **28**, 939 (2021).

[39] K. Klementiev and R. Chernikov, in *Proc. SPIE 9209, Advances in Computational Methods for X-Ray Optics III* (2014), p. 92090A.

[40] M. Stampanoni, A. Groso, A. Isenegger, G. Mikuljan, Q. Chen, A. Bertrand, S. Henein, R. Betemps, U. Frommherz, P. Böhler, et al., Proc. SPIE 6318, Developments in X-Ray Tomography p. 63180M (2006).

[41] T. Narayanan, M. Sztucki, T. Zinn, J. Kieffer, A. Holms-Puron, J. Gorini, P. V. Vaerenbergh, and P. Bosecke, J. Appl. Cryst. **55**, 98 (2022).

[42] J. W. Goodman, *Statistical optics* (Wiley-Interscience, New York, 1985).

[43] I. A. Vartanyants and A. Singer, New Journal of Physics **12**, 035004 (2010).

[44] H. Dierks and J. Wallentin, Opt. Express **28**, 29562 (2020).

[45] S. Zabler, P. Cloetens, J.-P. Guigay, J. Baruchel, and M. Schlenker, Review of Scientific Instruments **76**, 073705 (2005).

[46] J.-P. Guigay, Optik **49**, 121 (1977).

[47] L. Yang, S. Antonelli, S. Chodankar, J. Byrnes, E. Lazo, and K. Qian, J. Synchrotron Rad. **27**, 804 (2020).

[48] A. P. R. Eberle and L. Porcar, Curr. Opin. Coll. Interface Sci **17**, 33 (2012).

[49] R. Kádár, S. Spirk, and T. Nypelö, ACS Nano **15**, 7931 (2021).

[50] R. Kádár, A. Terry, K. Nygård, T. Nypelö, G. Westman, S. Wojno, R. Ghanbari, M. Fazilati, M. Bek, and A. K. Sonker, AIP Conf. Proc., Novel Trends in Rheology IX **2997**, 020007 (2023).

[51] K. J. Dobson, A. Allabar, E. Bretagne, J. Coumans, M. Cassidy, C. Cimarelli, R. Coats, T. Connolley, L. Courtois, D. B. Dingwell, et al., Frontiers in Earth Science **8**, 287 (2020).

[52] K.-J. Kim, *X-Ray Data Booklet* (Lawrence Berkeley National Laboratory, 2009), chap. 2.1, 3rd ed.

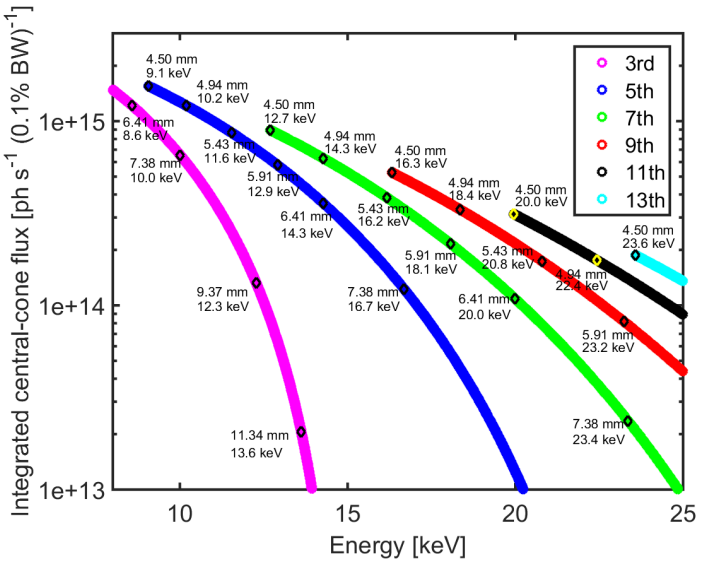

FIG. 1: Approximate integrated central-cone flux versus x-ray energy [52], shown for odd undulator harmonics. Selected insertion device gaps are specified for convenience.

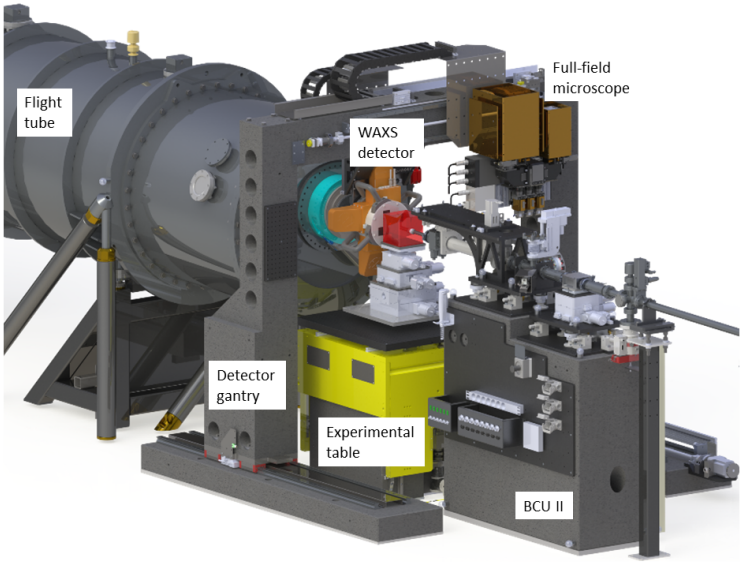

FIG. 2: Experimental station of the ForMAX beamline. The main components shown include the downstream BCU II, the experimental table, the detector gantry, with the WAXS detector and full-field microscope mounted onto it, and the evacuated flight tube, hosting the SAXS detector. In the SWAXS setup depicted in the figure, the vacuum nose cone, onto which the WAXS detector is mounted, is connected to the flight tube using a bellow, while the full-field microscope is translated out of the x-ray beam.

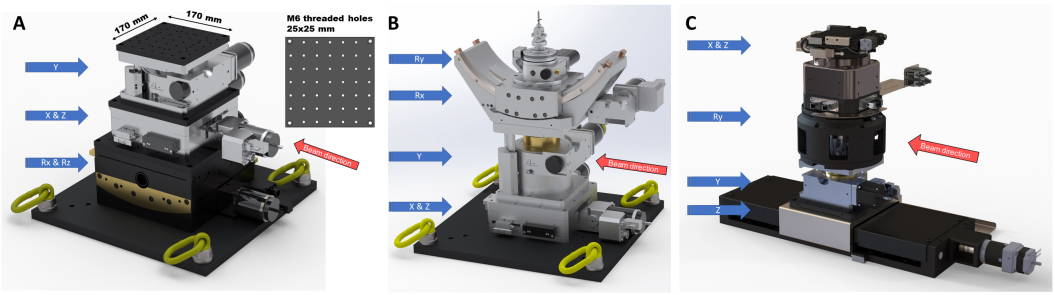

FIG. 3: Assembly of stages for sample manipulation in (A) SWAXS, (B) scanning SWAXS, and (C) SRμCT experiments.

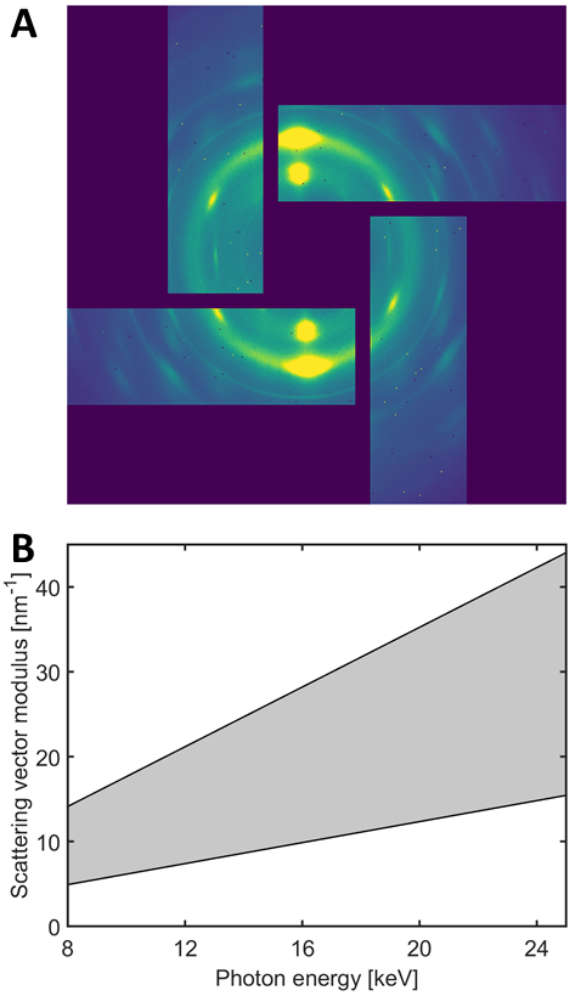

FIG. 4: WAXS at ForMAX using the custom Lambda 3M 'windmill' detector. Panel A exemplifies a diffraction pattern from a piece of wood, while panel B shows the nominal accessible range of scattering vector moduli q (gray area) versus x-ray energy.

TABLE I: Main parameters of the MAX IV 3 GeV storage ring.

Storage ring energy	3 GeV
Circumference	528 m
Beam current (operation November 2023)	400 mA
Projected beam current	500 mA
Electron beam emittance ($x \times y$)	326×8 pm^{2}rad^2
Electron energy spread	7.7×10^{-4}
Electron source size ($x \times y$)	54×4 μm^2
Electron source divergence ($x \times y$)	6×2 μrad^2
Top up	Every 10 minutes

TABLE II: Main components of the beamline.

Component	Distance from source [m]
Undulator	0
Front end movable mask	19.5
White-beam slits	23.9
Double multilayer monochromator	25.0
Double crystal monochromator	27.0
Vertically focusing mirror	30.2
Horizontally focusing mirror	31.0
Monochromatic slits	28.1, 32.3, 36.3, 41.5 - 41.8
X-ray prism lens (placeholder)	36.6
Compound refractive lenses	40.5
Experimental table	42.0
Full-field microscope	42.0 - 42.3
WAXS detector	42.1
SAXS detector	42.8 - 49.6

TABLE III: Main parameters of the undulator.

Magnet material	NdFeB
Pole Material	Vanadium permedur
Energy range	8-25 keV
Period length	17 mm
Number of periods	166
Minimum magnetic gap	4.5 mm
K value at minimum gap	1.89
Phase error	$\leq 2.5°$
Total power[a]	≈ 11.5 kW

[a]At projected 500 mA rung current.

TABLE IV: Hybrid photon-counting pixel detectors available at the beamline.

	Dectris	X-Spectrum
	EIGER2 X 4M	Lambda 3M
Number of pixels	4M	3M
Sensor size	2068×2162 pixels	$4 \times 516 \times 1536$ pixels
Pixel size	75×75 μm^2	55×55 μm^2
Sensor material	Si	Si
Sensor thickness	450 μm	320 μm
Dynamic range	32 bit	24 bit
Maximum frame rate[a]	560 Hz	1000 Hz
Data storage	Streaming	Streaming
Speciality	Vacuum compatible	'Windmill' shaped

[a]Full dynamic range.

TABLE V: sCMOS cameras available at the beamline.

	Hamamatsu ORCA Lightning	Andor Zyla 5.5	Photron FASTCAM Nova S16
Number of pixels	12M	5.5M	1M
Sensor size	4608 × 2592 pixels	2560 × 2160 pixels	1024 × 1024 pixels
Pixel size	5.5 × 5.5 μm^2	6.5 × 6.5 μm^2	20 × 20 μm^2
Dynamic range	16 bit	16 bit	12 bit
Maximum frame rate[a]	121 Hz	75 Hz	16 kHz
Data storage	Streaming	Streaming	128 Gb / 4 Tb

[a]Full frame and dynamic range.

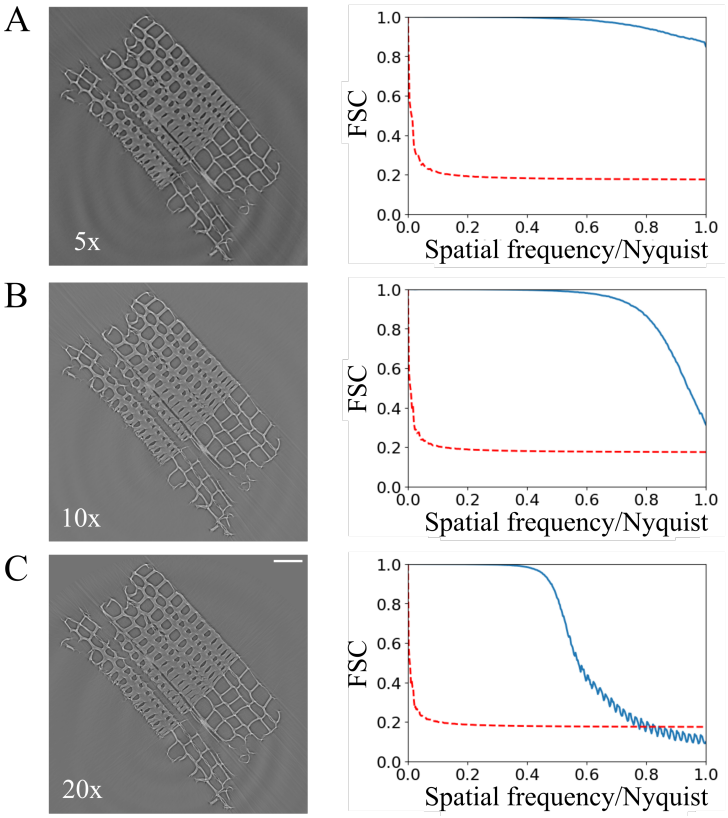

FIG. 5: SRμCT resolution evaluation at ForMAX. The left column contains the reconstructed slices for (A) 5×, (B) 10×, and (C) 20× magnification. The right column contains the results of the Fourier Shell Correlation (FSC) versus spatial frequency (normalized by the Nyquist frequency) for each of the magnifications (blue curve) and the half-bit error curve (dashed-red curve).

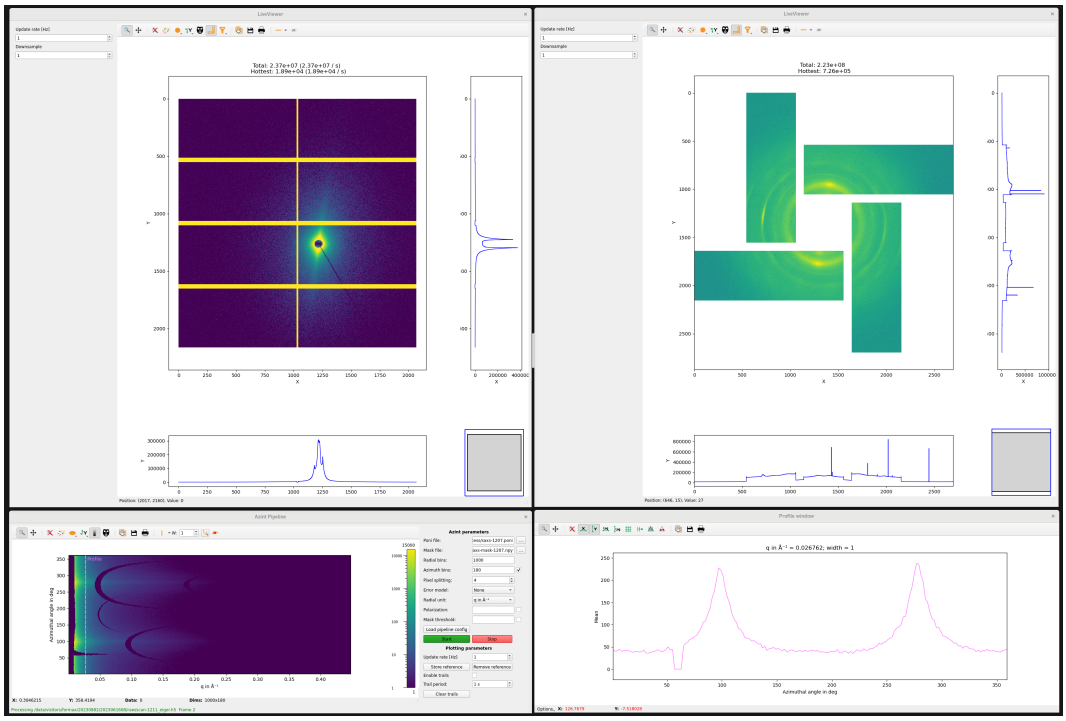

FIG. 6: Snapshot from the beamline control computer, exemplifying the live plotting of SWAXS data. The top panel shows as measured SAXS (left) and WAXS (right) data collected from a wood sample. The bottom left panel illustrates reduced 2D $I(q, \varphi)$ data in the SAXS regime. The line profile of the reduced 2D data, shown in the bottom right panel, corresponds to an annular integral of the as measured SAXS data and is convenient for monitoring anisotropy in the scattering data. Similar live plotting of reduced WAXS data is available at the beamline.

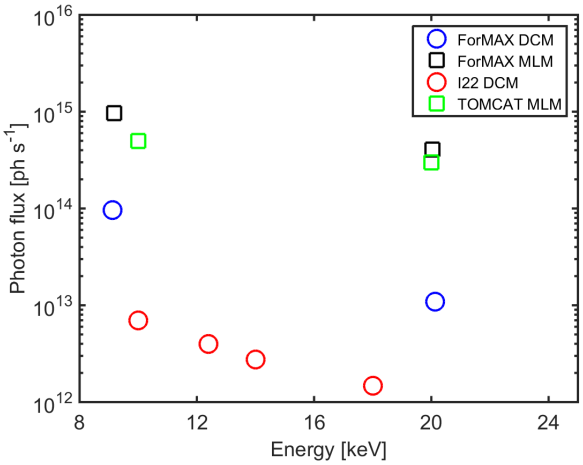

FIG. 7: X-ray photon flux at sample position versus x-ray energy, shown for both monochromators and selected x-ray energies. Corresponding data of the I22 and TOMCAT beamlines are also shown for comparison.

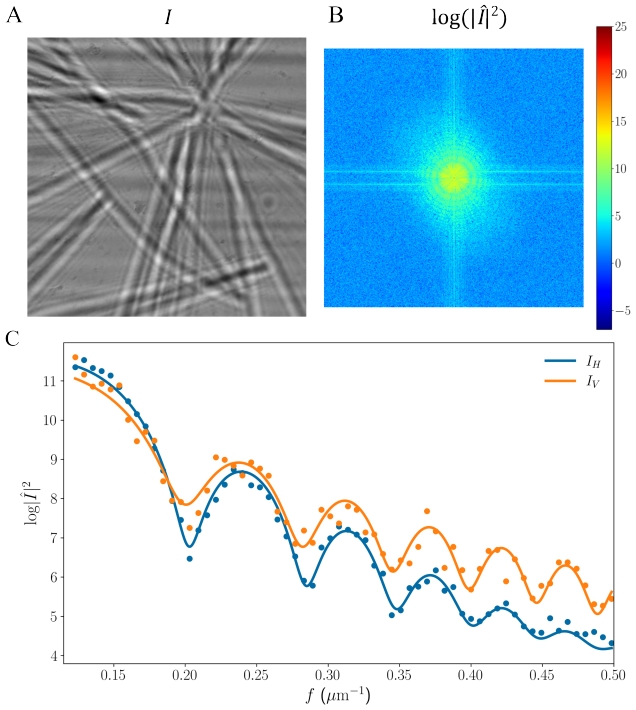

FIG. 8: Coherence evaluation via contrast-transfer-function analysis (CTF). (A) Hologram recorded from a broken Si_3N_4 membrane. (B) Power spectrum of the hologram in logarithmic scale ($\log|\hat{I}|^2$). (C) Lateral (blue symbols) and vertical (orange symbols) components of the power spectrum. The solid lines depict fits to the data.

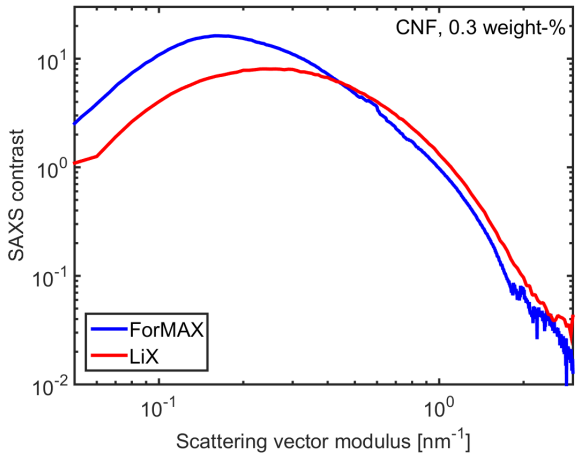

FIG. 9: SAXS contrast collected at ForMAX from highly charged, TEMPO-oxidized cellulose nanofibrils dispersed in water at low concentration of 0.3 weight-%. Corresponding data collected at the LiX beamline are also shown for comparison.

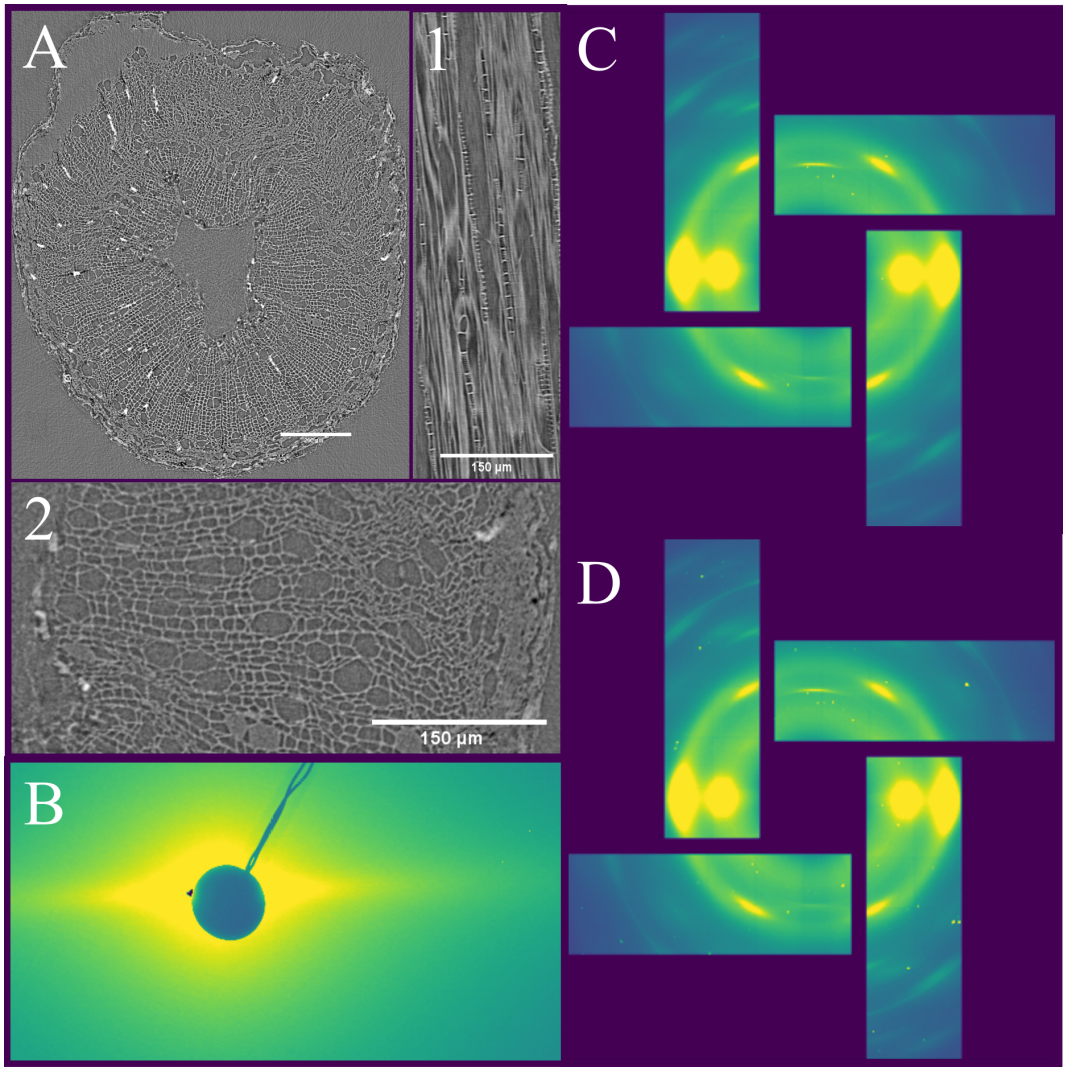

FIG. 10: Zooming into hierarchical materials at ForMAX. Panel A shows a 2D slice from the reconstructed 3D volume of an aspen sapling with a magnified view into cellular structure in both tangential (A1) and radial directions (A2) as obtained by SRμCT. Such data provide microscopic structural characterization and allows users to identify regions of interest for nanoscale mapping. Panels B and C-D present local SAXS and WAXS data, respectively, acquired using an x-ray beam focused to $\approx 25 \times 25$ μm^2 at the sample position. Panels C and D illustrate spatially resolved WAXS mapping of crystallites, measured at different positions within the sample.

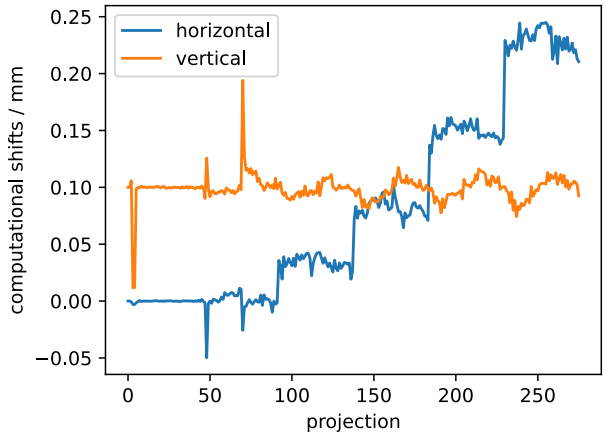

FIG. 11: Horizontal and vertical shifts as computed by the alignment procedure and applied to all projections before used as an input for the SASTT reconstructions via *Mumott*. Shifts are computed with the *phase_cross_correlation* function from the *skimage.registration* package in python with a Filtered-Back-Projection (FBP) tomogram from the measurement at 0° tilt as a reference.

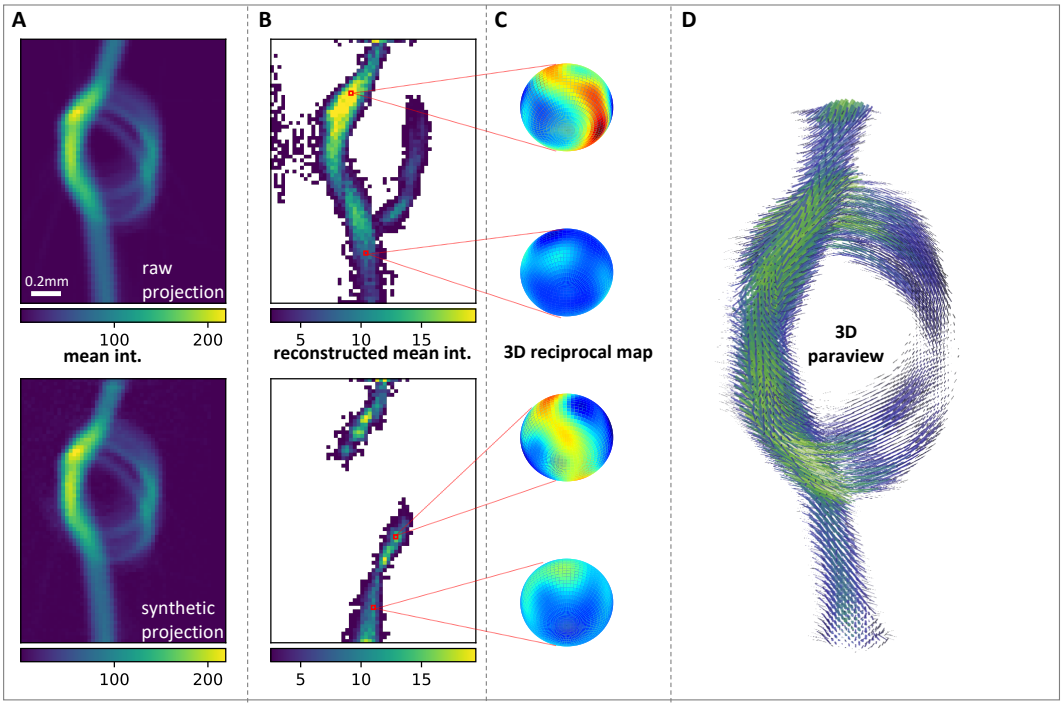

FIG. 12: Summary of SASTT analysis of a carbon fiber knot. Part A compares the mean intensity of a measured projection with the corresponding synthetic projection computed from the reconstruction. In B, two central cuts through the tomogram of the mean intensity (zx and zy slice) visualize the content of fibers throughout the tomogram. Four selected voxels are highlighted in red, for which the reciprocal space map is shown in C (interpolated with a five degree resolution and projected on a sphere). D presents a *ParaView* rendering of the knot.

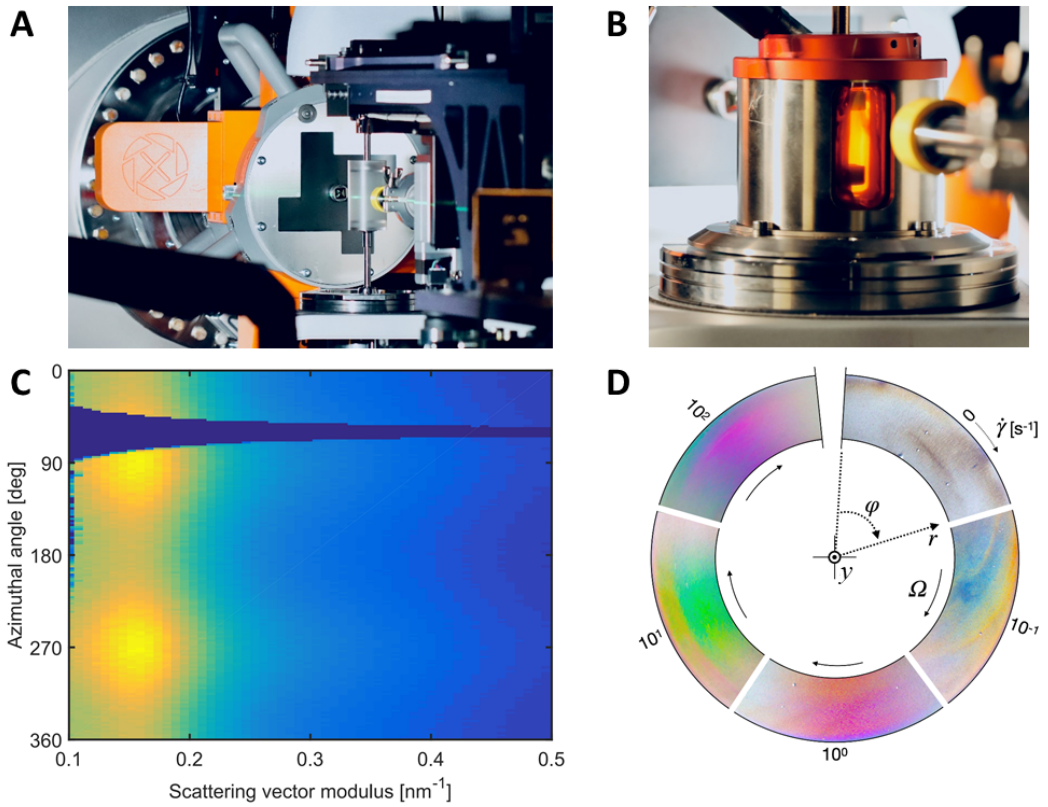

FIG. 13: Examples of *in situ* rheological and mechanical testing at ForMAX. Panels A and B show the Rheo-SWAXS and DMA-SWAXS setups at ForMAX, respectively, based on the Anton Paar MCR702 rheometer available at the beamline. The SAXS data of panel C collected from a suspension of cellulose nanocrystals (CNC), presented as a function of scattering vector modulus q and azimuthal angle φ, show nanoscale alignment of the suspension along the flow direction. Panel D illustrates *in situ* polarized light imaging of shear-induced mesoscale alignment in the xz plane of a CNC suspension as function of shear rate $\dot{\gamma}$, with the same flow geometry sector visualized clockwise with increasing $\dot{\gamma}$.